Types of spatter and their features and formation mechanisms in laser powder bed fusion additive manufacturing process

Zachary A. Young [a, b], Qilin Guo [b, c], Niranjan D. Parab [d], Cang Zhao [d], Minglei Qu [b, c], Luis I. Escano [b, c], Kamel Fezzaa [d], Wes Everhart [e], Tao Sun [f *], Lianyi Chen [a, b, c **]

[a] Department of Mechanical and Aerospace Engineering, Missouri University of Science and Technology, Rolla, MO 65409, USA

[b] Department of Mechanical Engineering, University of Wisconsin-Madison, Madison, WI 53706, USA

[c] Department of Materials Science and Engineering, University of Wisconsin-Madison, Madison, WI 53706, USA

[d] X-ray Science Division, Advanced Photon Source, Argonne National Laboratory, Lemont, IL 60439, USA

[e] Department of Energy's Kansas City National Security Campus Managed by Honeywell FM&T, Kansas City, MO 64147, USA

[f] Department of Materials Science and Engineering, University of Virginia, Charlottesville, VA 22904, USA

* Corresponding author

** Corresponding author

E-mail addresses: lianyi.chen@wisc.edu (Lianyi Chen), ts7qw@virginia.edu (Tao Sun)

Keywords: Spatter, Laser powder bed fusion, Additive manufacturing, High-speed imaging, Synchrotron x-ray

Abstract

Spatter causes defect formation, powder redistribution and contamination in laser powder bed fusion (LPBF) additive manufacturing process. It is critical to distinguish different types of spatter and understand their features and formation mechanisms. This work reveals the features and formation mechanisms of five unique types of spatter during the LPBF process by in-situ high-speed, high-energy x-ray imaging. Spatters observed during LPBF testing are quantified by their speed, size, and direction. Distinct quantifiable characteristics for each type of spatter are identified. Effects of the laser power, scan speed, and ambient pressure on spatter formation and features are unraveled. A spatter formation map for AlSi10Mg alloy is constructed.

1. Introduction

Laser powder bed fusion (LPBF) is an additive manufacturing technology that can manufacture metal parts with complex geometry [1–5]. Unfortunately, the spatters generated during laser-matter interaction have been witnessed to cause defects and part quality uncertainty [3–33], which severely limits the application of LPBF-manufactured parts.

To determine the cause of spatter formation, research has been conducted utilizing visible light and IR videography [20,22] and simulations [2,19,21,26]. Visible light and IR videography can monitor spatter moving behavior above the powder bed surface [17,21,22]. However, they lack the ability to see through the metal powder bed, so the accurate determination of spatter formation mechanisms is difficult from the information acquired only above the powder bed surface. Simulations can model the melt pool which has revealed important physical mechanisms of spatter formation [34]. Currently, simulations are hard to, however, accurately model the spatter formation resulting from the complex interplay of metal vapor plume and ambient gas flow.

Recently, we showed that high speed x-ray imaging can overcome the limitations of conventional characterization tools to reveal the dynamics of spattering behavior during LPBF process [18]. We revealed spattering dynamics as a function of time, pressure, and location throughout the manufacturing process. However, our previous work did not distinguish different types of spatter.

In this work, we conduct hundreds of tests at varying laser parameters and environment conditions to obtain detailed insight into the types of spatter and their features and formation mechanisms. This work identifies five unique types of spatter that exist within the LPBF process. The formation mechanism of spatters has been determined and/or discussed. The size, speed, and direction have been quantified. The effects of the laser power, scan speed, and ambient pressure on spatter formation are studied. A spatter formation map for AlSi10Mg alloy is constructed.

2. Material and Method

High-speed high-energy x-ray imaging (Beamline 32-ID-B, Advanced Photon Source, Argonne National Laboratory) was used to monitor the dynamics of spattering during the laser melting process. The experiments were first recorded at a frame rate of 45,259 fps (frames per second) to primarily determine physical characteristics of the phenomena. Then, a high frame rate of 135,776 fps was used to capture the detailed process of how certain phenomena form. ImageJ is used for image processing throughout the experimental data analysis.

An IPG continuous-wave (CW) ytterbium fiber laser (IPG YLR-500-AC, IPG Photonics, Oxford, USA) with a wavelength of 1070 nm and a maximum output power of 520W was used to melt the material. A laser scanner (IntelliSCANde 30, SCANLAB GmbH., Germany) is used to control laser scan speed. A laser beam incident angle of 90 degrees is used for all testing. The laser scan path is a single continuous scan of 3-4 mm perpendicular to the x-ray beam.

Powder layers (about 100 µm) are spread on a metal substrate with identical composition to the powder. Two pieces of glassy carbon are mounted as side walls to hold the powder in place. The powder layer thickness is determined by the difference in height between the substrate and glassy carbon. Both aluminum alloy (AlSi10Mg, 15-38 µm powders with alloying elements of 9-11% silicon, 0.25-0.45% magnesium, and less than 0.25 of iron, nitrogen, oxygen, titanium, zinc, manganese, nickel, copper, lead, and tin) and titanium alloy (Ti6Al4V, 25-45 µm powders with alloying elements of 5.5-6.5% aluminum, 3.5-4.5% Vanadium, and less than 0.25 oxygen, nitrogen, carbon, hydrogen, and iron) were tested in our work. Testing is conducted in a vacuum chamber filled with argon gas (99.99%). Environmental pressure is varied from the region of near vacuum (0.002 atm) to atmospheric (1 atm) to observe the effects of ambient pressure.

3. Results and discussion

3.1. Identification of spatter types and formation mechanisms

Five types of spatter were identified through in-situ analysis of the LPBF process. The spatter formation dynamics is captured and analyzed to determine their individual formation mechanisms. The five types of spatter and their formation mechanisms are discussed in detail below.

3.1.1. Solid spatter

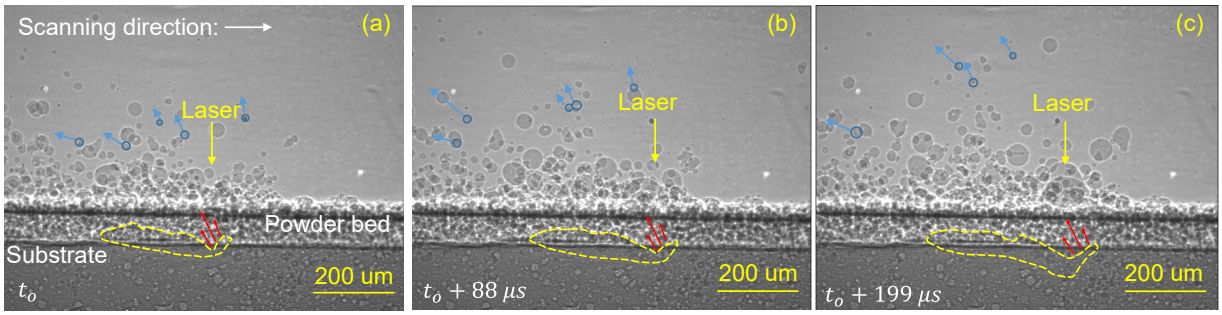

Fig. 1. Solid spatter. *Dynamic X- ray images showing dynamics of solid spatter when a laser beam with a diameter of 100 um and power of 322 W scans a powder bed with a layer thickness of 100 µm at a scan speed of 0.8 m/s. Yellow arrow and dashed line indicate the position of the laser beam and the melt pool boundary, respectively. Blue circles and arrows indicate the representative solid spatters ejecting from the substrate over time. Red arrows indicate the hypothesized vapor jet direction.*

During scanning, powder is observed to be ejected prior to sufficient laser interaction to induce melting. Large amounts of un-melted spatter are seen throughout the entire scanning process. This type of un-melted spatter is referred to as solid spatter. The solid spatter generation is caused by the vapor jet (intense vapor generated due to localized laser heating) interacting with solid powder outside the strong laser interaction region. The vapor jet can create sufficient force to eject un-melted powders before melting can take place. Fig. 1 shows the dynamics of the vapor jet ejecting un-melted powders away from the melt pool. The details about the vapor jet induced spatter phenomena can be found in our previous publication [18]. Solid spatter formation can lead to non-uniformity in powder layer thickness but has less detrimental effects on the overall part quality compared to liquid spatter [5,19–22,27].

3.1.2. Metallic jet

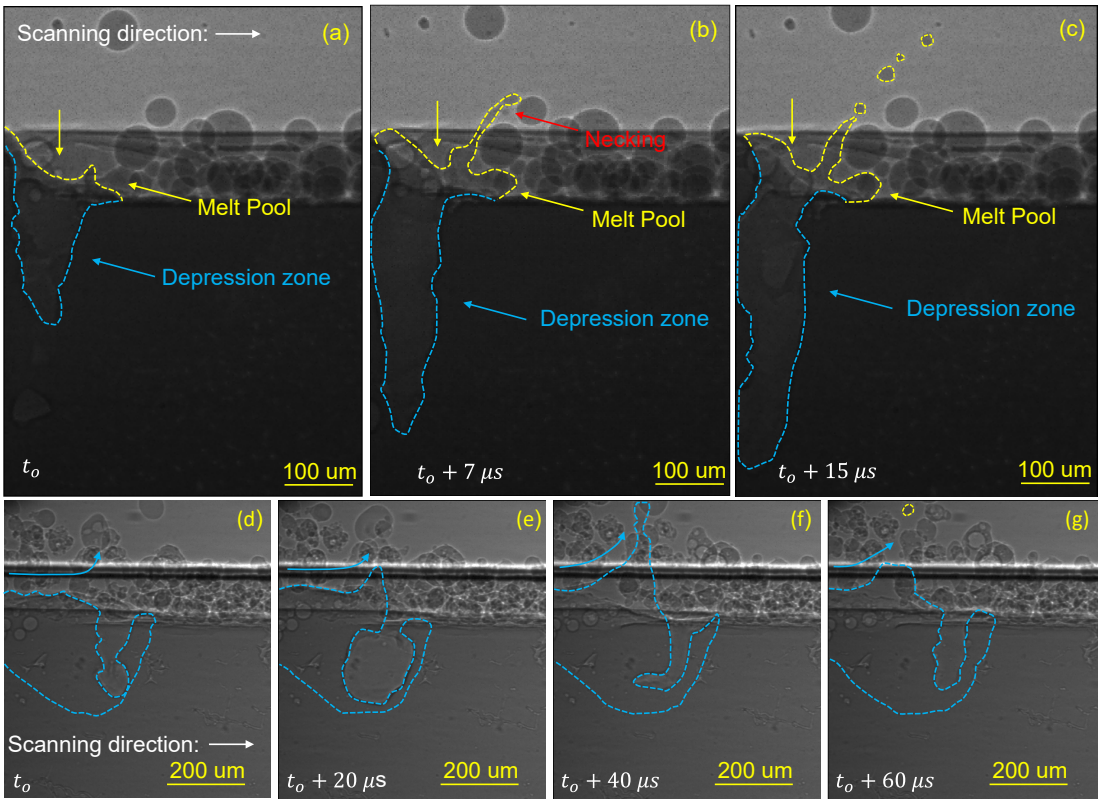

Fig. 2. Metallic jet spatter. *Dynamic X-ray images demonstrating front metallic jet spatter formation (a-c) and rear metallic jet formation (d-g). (a,d) Protrusion formation at the edge of the depression zone region. (b,e) Lengthening and necking of the protrusion. (c,f) Breaking of the neck to form liquid droplet (spatter). The rapid increase of the depth or the width of the depression zone was observed during the spatter formation process, which indicates that the rapid depression zone volume expansion can cause the spatter formation. The depression zone and top of the melt pool boundaries are marked in blue and yellow dashed lines, respectively. In a-c. The material is Ti6Al4V, laser power is 260 W, scan speed is 0.2 m/s. In d-f, the material is AlSi10Mg, laser power is 416 W, scan speed is 0.5 m/s.*

Liquid droplets are observed to be ejected from the melt pool at the edge of the depression zone region. This type of spatter is referred to as metallic jet spatter. The formation of the metallic jet spatter is caused by the intense metallic vapor during the localized laser heating process. The intense metallic vapor generates high recoil pressure and shear forces on the depression zone's vapor-liquid interface during the LPBF process. The recoil pressure creates strong melt flow along the depression zone walls. The intense vapor flow also generates shear forces on the depression zone wall, contributing to high speed spatter upward from the melt pool. When the metallic vapor is intense enough to produce forces capable of overcoming the surface tension, necking of the melt pool begins to appear on the walls of the depression zone (Fig 2, b,f) and leads to the liquid detachment from the elongated melt pool protrusion (Fig. 2, c,g). Our recent results show that bulk-explosion is also an important mechanism for metallic jet formation [11]. The production of metallic jet spatter is reliant on the intensity of the vapor jet and stability of the depression zone; this makes unstable depression zones more prominent in the production of metallic jet type spatters.

3.1.3. Powder agglomeration spatter

Powders and spatters are observed to agglomerate and coalesce to form spatters many times larger than the original feedstock powder. This type of spatter is referred to as powder agglomeration spatter. Two main kinds of powder agglomeration spatter are commonly observed in the experiment: liquid-solid powder agglomeration and liquid-liquid powder agglomeration.

Liquid-solid powder agglomeration spatter is seen as feedstock powders being melted near the melt pool region but not being captured and absorbed by it. Two vapor streams contribute to the agglomeration spatter: the vapor from the localized vaporization of the rear size of the powder and the vapor plume from the depression zone. The laser beam heats the rear side of the powder/spatter, which generates a vapor stream pushing the liquid ball away from the laser beam approximately along horizontal direction [34]. The liquid ball then travels along the powder bed region (Fig. 3a) and captures more un-melted feedstock powders (Figs. 3b-c) along its path to grow, very similar to the growth of a snowball. Then, the vapor jet from the depression zone ejects the liquid ball out of the powder bed (Fig. 3c) to form a big spatter.

Liquid-liquid powder agglomeration spatter is the coalescence of two liquid spatter particles by colliding. Figs. 3(d-f) show one example. Two independent liquid spatters are ejected away from the melt pool (Fig. 3d). During ejection, the two powders collide (Fig. 3e) causing the liquid spatters to coalesce into a single, larger spatter (Fig. 3f).

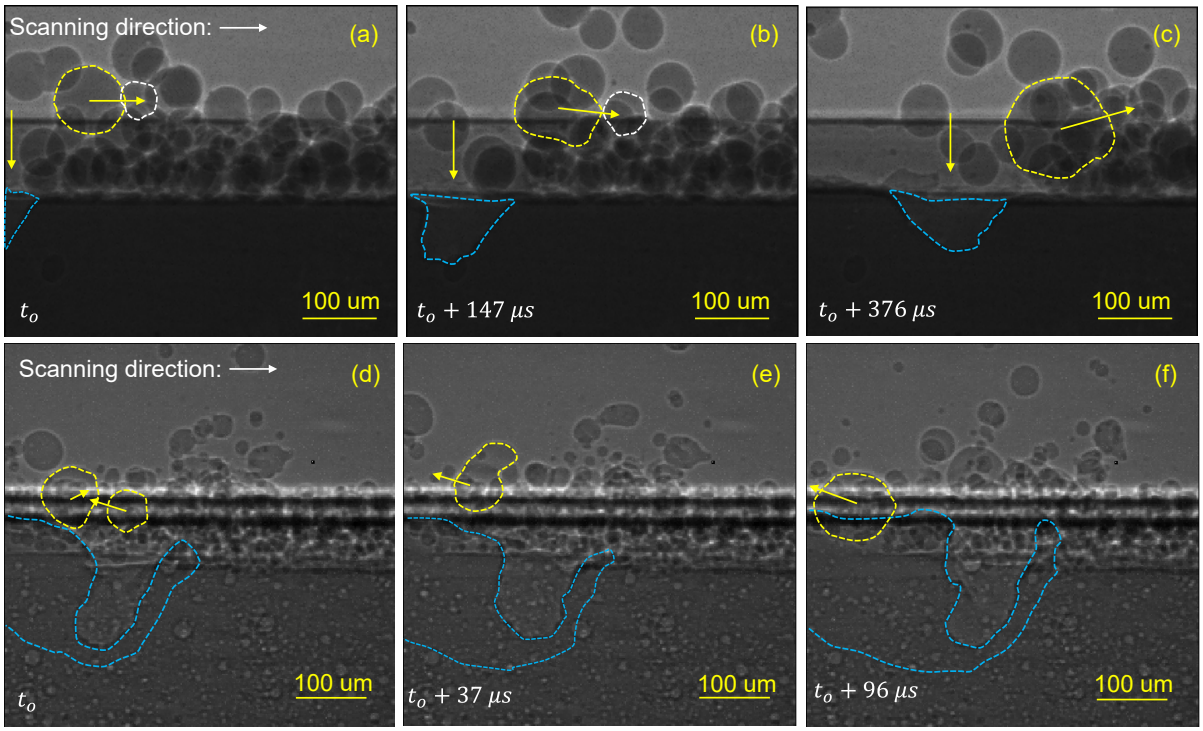

Fig. 3. Powder agglomeration spatter. *(a-c), Dynamic X-ray images demonstrating liquid-solid powder agglomeration spatter. Liquid droplets and solid feedstock powder prior to absorption are indicated by yellow and white dashed lines, respectively. (a) A liquid droplet (indicated by yellow dashed circle) is pushed forward (the powder that will be absorbed by the liquid droplet is indicated by white dashed circle). (b) The liquid droplet and powder indicated in (a) merged together to form a larger liquid ball (indicated by yellow dashed circle in b). The newly merged liquid ball was pushed towards another powder in the powder bed (indicated by the white dashed circle). (c) The liquid ball grows to multiple times larger than the size of the feedstock powder by absorbing multiple feedstock powders, and then is ejected away by the vapor jet from the depression zone. (d-f), Dynamic X-ray images demonstrating liquid-liquid powder agglomeration spatter. (d) Initially melted powder droplets were ejected with different moving directions. (e) Then, the two liquid droplets collide and merge. (f) Finally, the combined droplet ejects from the melt pool region. In (a-c), the material is Ti6Al4V, laser power is 312W, laser scan speed is 0.6 m/s. In (d-f), the material is AlSi10Mg, laser power is 416W, scan speed is 1.0 m/s. Melt pool boundaries are indicated by blue dashed lines.*

3.1.4. Entrainment melting spatter

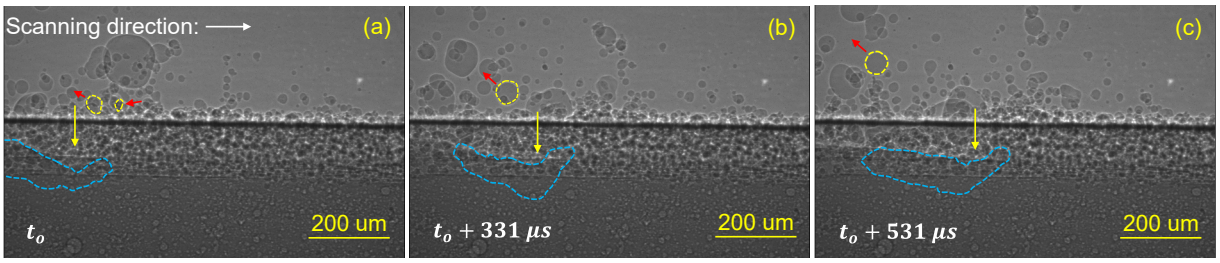

Fig. 4. Entrainment melting spatter. *Dynamic X-ray images demonstrating entrainment melting spatter. (a) Two spatters get entrained towards the laser heating region. (b) The two spatters melt and coalesce in the laser heating region forming a single liquid droplet. (c) The liquid droplet was ejected away from the laser. The laser beam diameter is 100 um, laser power is 416W, scan speed is 0.4 m/s. The material is AlSi10Mg. The dashed yellow circles indicate the tracked spatters. The yellow arrow marks the location of the laser beam. The red arrow marks the moving direction of the spatter. The blue dashed lines indicate the melt pool boundary.*

Ambient gas flow can carry powders to the laser heating region, also known as powder entrainment. Once the entrained solid powders encounter the laser beam, the solid powders are melted (Fig. 4 a,b) and ejected by the vapor jet (Fig. 4c). Sometimes, the melted entrained powders can collide and coalesce (Fig. 4 a,b). This type of spatter is referred to as entrainment melting spatter.

3.1.5. Defect induced spatter

X-ray imaging demonstrates that when the laser interacts with severe defects within the part such as large pores, a sudden eruption of liquid spatter can occur. During melting, laser interaction with these large pores exhibits sudden instability and results in unique spatter. This type of spatter is termed as defect induced spatter. Fig. 5 demonstrates an example of defect induced spatter recorded using x-ray imaging. During laser scanning, the melt pool comes into contact with a large pre-existing pore (Fig. 5a). The large pore interacts violently with the melt pool to cause the formation of liquid spatter (Fig. 5c). The rapid expansion of the trapped gas in the pore and/or the rapid change of the absorbed laser energy by multiple reflections in the pore are possible mechanisms for defect induced spatter.

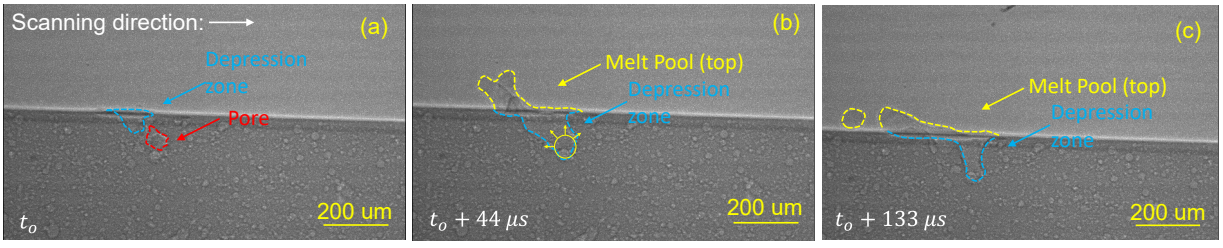

Fig. 5. Defect induced spatter. *Dynamic X-ray images demonstrating an example of defect induced spatter. (a) The depression zone travels along the substrate towards a large pre-existing pore. (b) The interaction between melt pool/depression zone with the localized defect cause a sudden eruption out of the melt pool. (c) A large liquid droplet detaches from the melt pool to form a spatter. The material is AlSi10Mg, laser beam size is 100 um, laser power is 416 W, scan speed is 1.0m/s. The pre-existing pore and depression zones are outlined by dashed red and blue lines, respectively. The sudden melt pool instability and resulting spatter are highlighted in yellow for all images.*

3.2. Schematic of spatter formation mechanisms

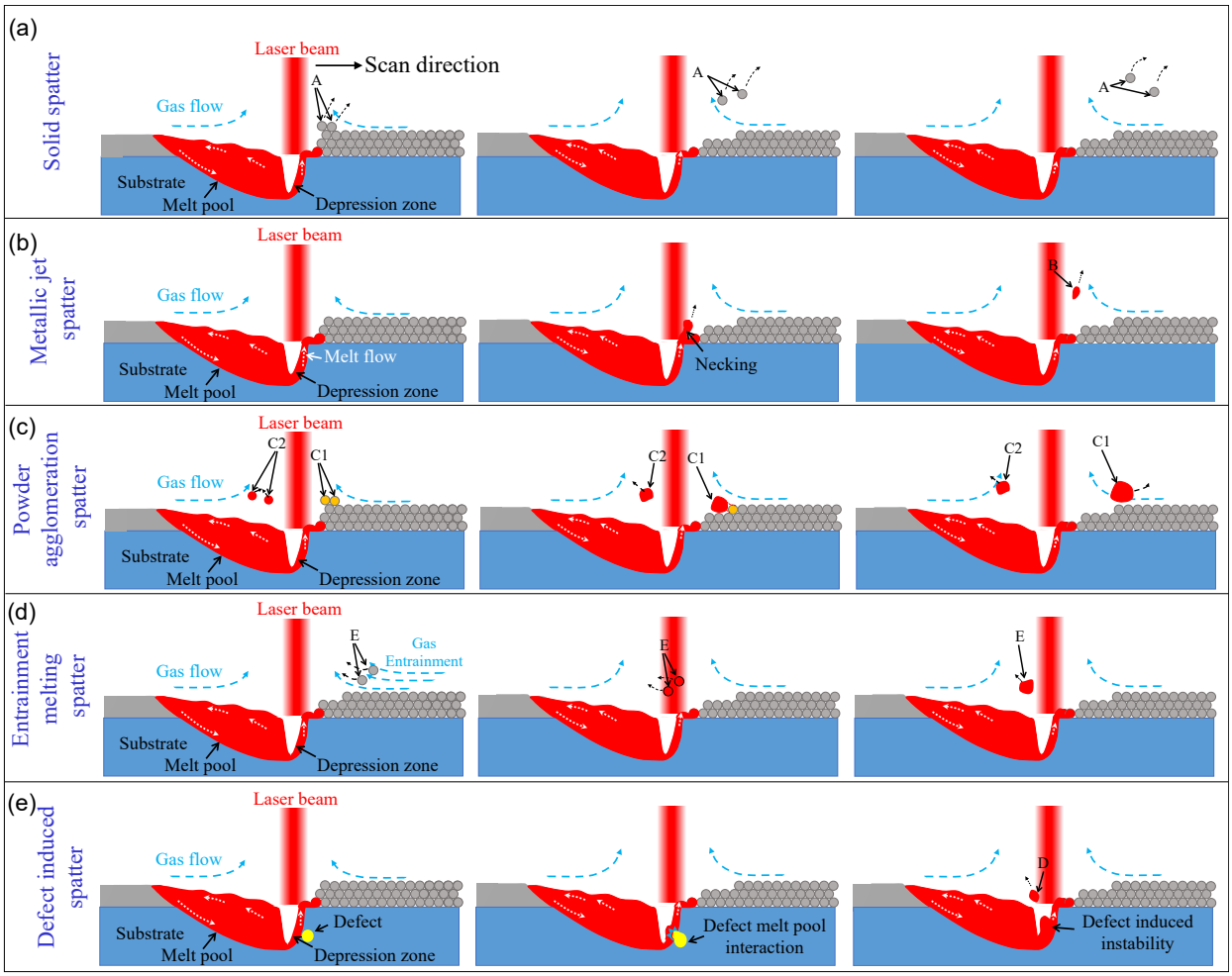

Fig. 6. Schematic showing the formation mechanisms of all spatter types. *(a) Solid spatter (A). (b). Metallic jet spatter (B). (c). Powder agglomeration splatter (C1, liquid-solid agglomeration spatter, C2, liquid-liquid agglomeration spatter). d. Entrainment melting powder spatter (D). (e). Defect induced spatter (E).*

To better visualize and understand spatter in the LPBF process, a schematic was constructed to summarize the spatter types and their formation mechanisms, as shown in Fig. 6. The formation dynamics of solid spatter, metallic jet spatter, powder agglomeration spatter, entrainment melting spatter and defect induced spatter are pointed out by A, B, C (C1 and C2), D and E, respectively.

3.3 Quantification of spatter features

The size, speed and direction of the spatters are different due to their different formation mechanisms. Quantification are done by frame by frame manual powder tracking of individual spatter to maintain accuracy and ensure minimal error. Solid spatter will always remain constant in size due to no melting during ejection. Defect induced spatter is difficult to be quantified statistically due to the low number and randomness of pre-existing pores within tested substrates. As a result, these two types of spatter were not included in the quantification study of their spatter features. All quantitative testing was conducted with aluminum for the consistency of comparison.

3.3.1. Spatter speed and size

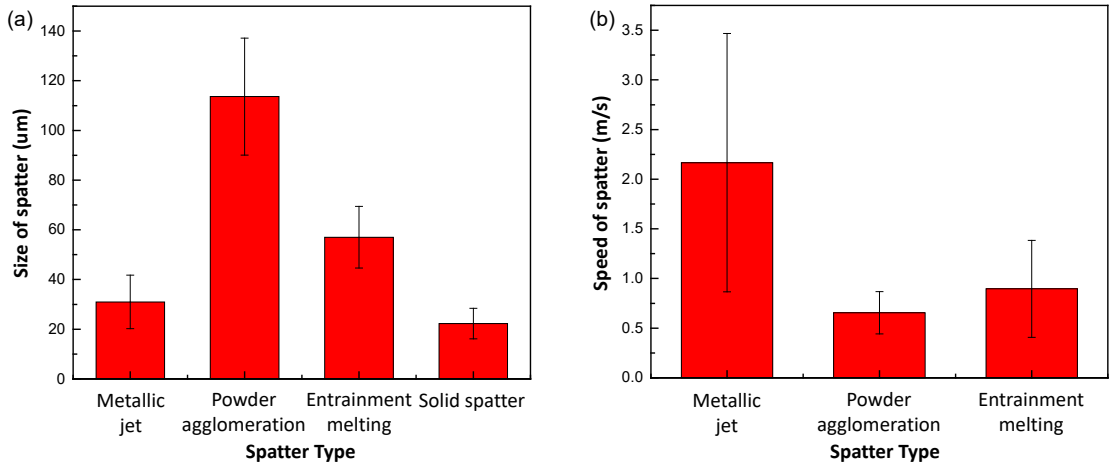

Fig. 7. Quantification of the speed and size of spatter. *(a) Spatter speed (projected on the 2D imaging plane). (b) Spatter size. The material is AlSi10Mg. The error bar indicates standard deviation. Spatter phenomena are determined and collected from multiple videos under varying scanning speeds and laser powers.*

The speed of the powders was quantified individually by recording the change in position of the object's geometric center over intervals of time. The standard deviation is taken from the variation of the average speeds generated by the particles observed and quantified. Average speeds of three types of spatter were determined and compared (Fig. 7a). The metallic jet was determined to be the fastest of the four phenomena, with an average speed of 2.17 m/s. Entrainment melting spatter moves faster than powder agglomeration spatter due to the large size difference or an initial velocity prior to melting. The powder agglomeration spatter followed behind the entrainment melting spatter with an average speed of 0.66 m/s. The standard deviation of the metallic jet is 1.30 m/s. The large variation in speed is caused by multiple spatters being ejected from the same protrusion; the initial ejected spatter has greater speed than the subsequent spatter.

The size of the four types of spatter are quantified (Fig. 7b). As expected, the solid spatter has the same size as the feedstock powder. The powder agglomeration spatter has the largest size with an average diameter of 114 μm, which is over 4 times larger than the feedstock powder. The entrainment melting spatter has a size of 57 μm in diameter, which is about 3 times larger than the feedstock powder. The metallic jet spatter's size is with an average size of 31 μm, which is close to the size of the feedstock powder.

The speed and size of the spatter not only depend on the formation and ejection mechanisms, but also depend on the material properties and processing parameters. The value of the spatter data shown in Fig. 7 might not be generalized to other materials or other processing conditions.

3.3.2. Spatter direction

Quantifying the moving directions of the different types of spatters were conducted. The results showed a general trend that the moving direction of the metallic jet spatter makes the smallest angle with the laser beam and the moving direction of the powder agglomeration spatter makes the largest angle with the laser beam. However, the moving direction of spatter varies in a very large range and strongly depends on processing parameters.

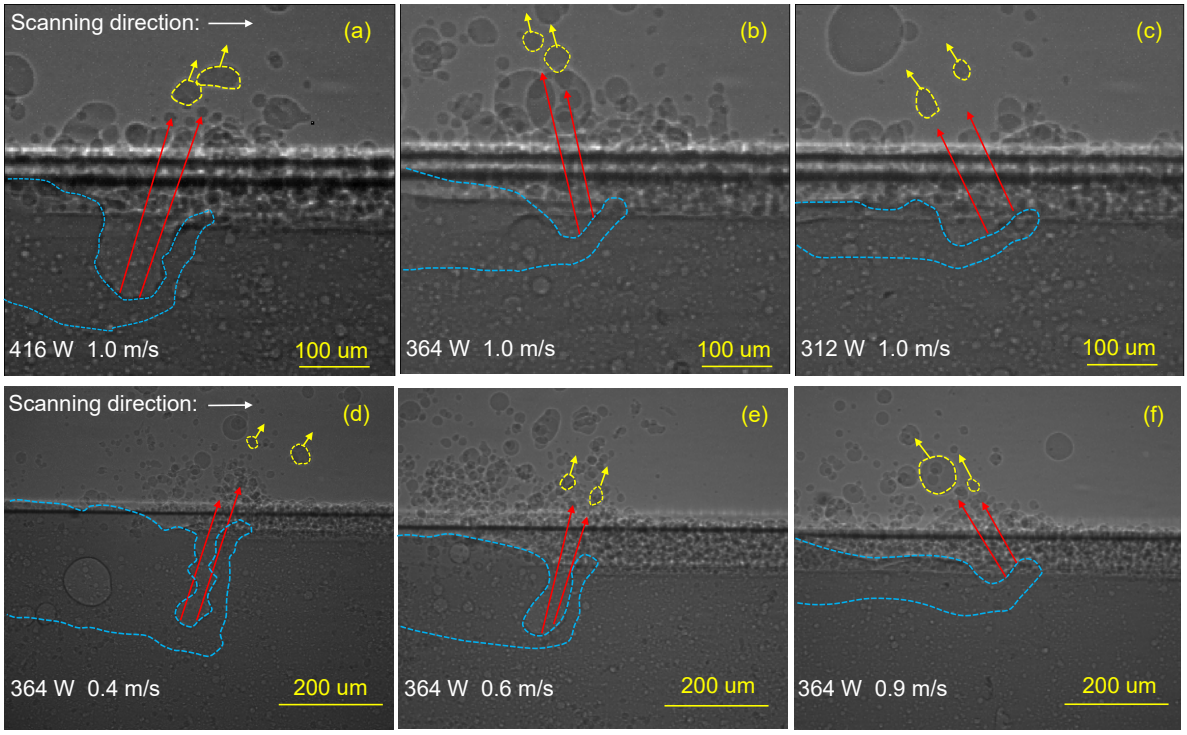

Fig. 8. Effects of processing parameters on direction of spatter. *(a-c) X-ray images demonstrating the effects of laser power on spatter direction and depression zone geometry. (d-f) X-ray images showing the effects of scan speed on spatter direction and depression zone geometry. Melt pool and spatter are outlined by blue and yellow dashed lines, respectively. Red arrows indicate the hypothesized vapor jet direction. The material is AlSi10Mg.*

The dependence of the spatter direction on processing parameters originates from the effect of processing parameters on vapor jet direction, as shown in Fig. 8. Changing the laser power at a constant laser scan speed (Fig.8 a-c) or changing the scan speed at a constant laser power (Fig. 8 d-f) can significantly change the depression-zone geometry. The depression zone changes from a deep keyhole shape (with a depth over half width ratio larger than one) at high laser power and low scan speed to a wide open shape (with a depth over half width ratio less than one) at low laser power and high scan speed. Consequently, the vapor jet direction changes from nearly parallel to the depression zone front wall to nearly normal to the depression front wall. Since vapor jet is the major driven factor for spatter formation and moving, the spatter direction changes accordingly.

Due to the strong dependence of spatter direction on processing parameter, it is very hard to make a quantitative comparison among different types of spatters. However, the correlation among the spatter direction, depression-zone shape and laser processing parameter has important implications for developing in-situ monitoring tools based on spatter characteristics.

3.4. Effects of processing parameter on spatter formation and mitigation

During quantification, isolating the effects of different processing parameters delivered some dramatic changes to different spatter phenomena. Changes to different dynamics within the melt pool and surrounding region lead to mitigation or elimination of different spatter types. Testing was conducted to determine the regions where laser power, scan speed, and ambient pressure induce mitigation or elimination of the observed spatter types. The results are described below.

3.4.1 Effect of laser power and scan speed on spatter formation and mitigation

Laser power and scan speed play important role in spatter formation. The effects of laser power and scan speed on the formation of different type of spatters are summarized in Fig. 9.

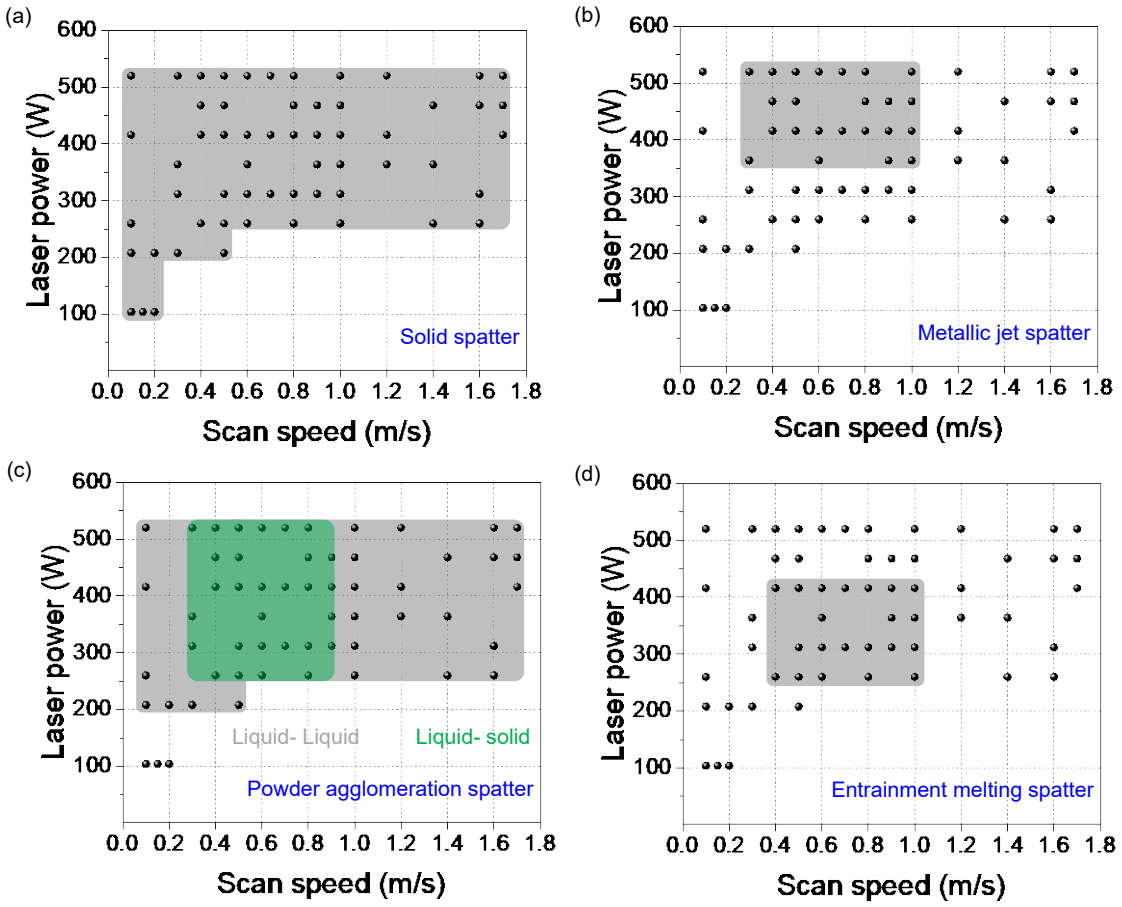

Fig. 9. Charts showing spatter formation under various processing conditions (spatter formation map). *(a) Solid spatter. (b) Metallic jet spatter. (c) Powder agglomeration spatter. (d) Entrainment melting spatter. The material is AlSi10Mg. Black dots indicate the parameters tested. The shaded areas indicate the area that a specific type of spatter was observed. All outlines are generated by observations of spatter from our testing at specified processing conditions and are not verified as thresholds or absolute boundaries where the specific spatter types are capable to form.*

Solid spatter was witnessed during all laser power and scan speed conditions tested (Fig. 9a). Solid spatter is produced through vaporized metal ejecting un-melted powder away from the substrate. Our testing was conducted only when melting could occur, so elimination of solid spatter was not possible. Solid spatter mitigation is witnessed slightly by reducing the laser power or increasing the scan speed to reduce the overall energy density. The decrease in energy density reduces the strength of the vapor jet preventing more solid spatter from being ejected.

Metallic jet spatter was observed within a specific laser power and scan speed range (Fig 9b). Elimination was seen by reducing the laser power or by increasing the scan speed above certain threshold. Reduction in laser power (below 364 W) or increase in laser scan speed (greater than 1 m/s) decreases the input energy density. This energy density decrease causes the vapor jet and melt flow strength to be insufficient to produce metallic jet spatter. Decreasing the scan speed (below 0.3 m/s) was also observed to eliminate the production of metallic jet spatter for AlSi10Mg. At the reduced scan speed, the resulting depression zone becomes a deep keyhole. When the keyhole is very deep, the highest intensity of the melt flow is at the bottom of the melt pool. The high intensity

melt flow weakens as it travels up the depression zone walls. The resulting momentum of the liquid on the keyhole rim is then not high enough to form long protrusion that can be detached from the melt pool.

Liquid-liquid powder agglomeration spatter was witnessed during all laser power and scan speed conditions tested (Fig. 9c). The inability to prevent liquid-liquid powder agglomeration is due to the incorporation of feedstock powders interacting with laser heating. Like solid powder, the melted powder is ejected by the vapor jet. The only occurrences where liquid-liquid powder agglomeration is not present is in the absence of noticeable melting needed for LPBF.

Liquid-solid powder agglomeration spatter elimination, however, was possible by tuning the laser power and scan speed (Fig. 9c). At high scan speed (e.g., above 0.9 m/s), the laser scan speed/melt pool moving speed could overtake the speed of the agglomerating spatter and capture it within the melt pool preventing ejection. At low scan speed (e.g., below 0.3 m/s), the generated vapor jet was too strong relative to the ambient gas flow causing liquid spatter to not be pushed into the un-melted feedstock but, rather, eject as liquid-liquid powder agglomeration spatter instead. Liquid-solid powder agglomeration spatter can be many times larger than many of the other types of spatter, so the ability to eliminate the liquid-solid powder agglomeration spatter from the process is vital for improving build quality.

Entrainment melting spatter only occurred within a small region of the laser processing conditions during testing (Fig. 9d). The occurrence of entrainment melting spatter is strongly related to force generated by the ambient gas flow and vapor jet. Testing above 416 W laser power generated a vapor jet that was too powerful for entrained solid spatter to overcome the outward force and interact with the laser heating region. This phenomenon was also present when operating below 0.4 m/s. The vaporized material buildup at lower speeds was too strong for entrained solid powders to reach laser heating before being ejected. Testing done at speeds higher than 1.0 m/s caused entrained powders to not interact within laser heating region long enough to induce melting or not be able to move to the laser heating region to induce melting.

3.4.2. Effects of environment pressure on spatter formation and mitigation

Environment pressure has a great influence on spatter formation, as shown in Fig. 10. Two spatter types were primarily affected by the reduction in the environmental pressure: solid spatter and entrainment melting spatter.

Solid spatter occurred at every LPBF testing when manipulating laser power, scan speed, or environmental pressure. The solid spatter was, however, substantially affected by environmental pressure. When the pressure was reduced from 760 Torr (Fig 10a-c) to 0.087 Torr (Fig 10d-f), the resulting solid spatter was substantially increased. Under vacuum, there is no ambient pressure to counteract the vaporization pressure produced during melting causing an increase in solid spatter in all direction [20]. Higher pressure confines the metallic vapor jet in a narrower region, resulting reduction of solid spatter.

Entrainment melting spatter generation requires the presence of ambient gas flow as its primary mechanism for solid spatter entrainment. The reduction of ambient pressure from 760 Torr to 0.087 Torr makes the ambient gas flow too low to cause powder entrainment . The inability for solid spatter to be entrained causes the elimination of entrainment melting spatter when operating in near vacuum conditions.

Liquid-solid powder agglomeration spatter also requires the assistance of ambient gas flow to keep the agglomerating spatter from immediately being ejected. Without strong ambient gas flow, powder directly melted from the laser immediately escape due to the vaporization pressure. Reducing the environmental pressure from 1 atm to 0.087 Torr eliminated the production of liquid-solid powder agglomeration spatter. Unfortunately, liquid-liquid powder agglomeration spatter was unable to be eliminated by the reduction of environmental pressure.

The alteration in the environmental pressure was unable to eliminate the production of metallic jet spatter. The presence of metallic jet spatter was still witnessed even under near vacuum condition. The alteration in the environmental pressure was also unable to eliminate the production of defect induced spatter. Defect induced spatter is generated specifically from the incorporation of defects and no visible evidence was found to show mitigation or elimination of defect induced spatter due to changes in environmental pressure.

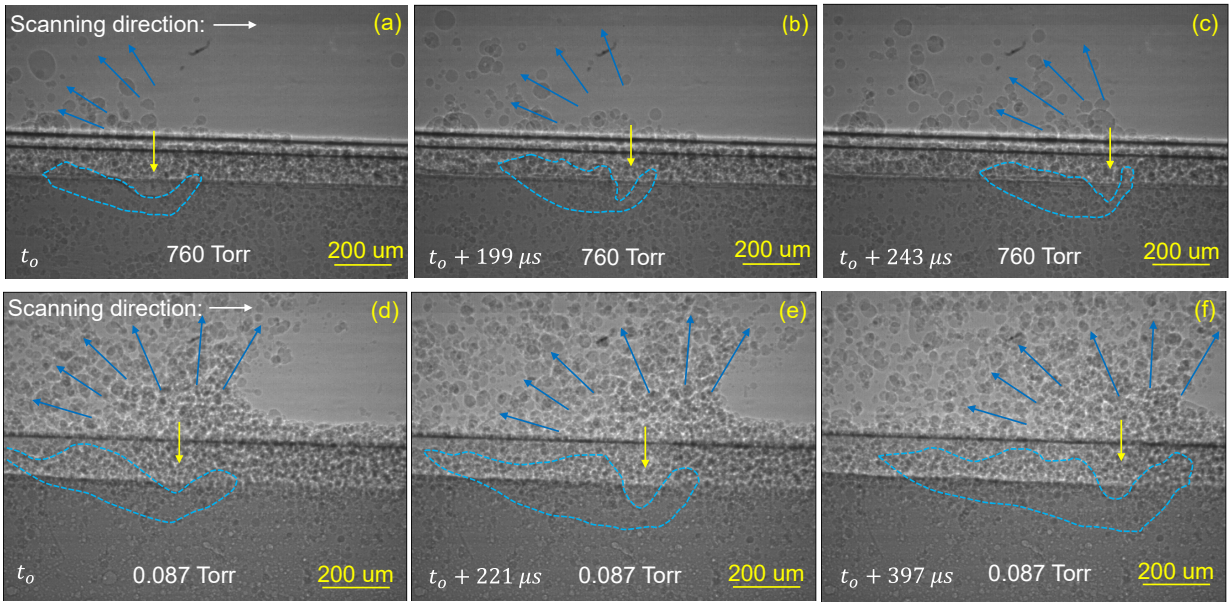

Fig. 10. Effect of atmosphere pressure on spatter behavior. *(a-c), Dynamic x-ray images showing spattering behavior under 760 Torr (1 atm). (d-f) Dynamic x-ray images showing spattering behavior under 0.087 Torr (0.00132 atm). The laser power is 416 W, beam size is 100 µm, scan speed is 1.0 m/s. The yellow arrow indicates the current location of the laser beam. The blue dashed lines indicate the melt pool boundaries. Quantity and direction of solid and liquid spatter can be easily identified from regions marked with blue arrows.*

3.4.3 Effects of material feedstock on spatter formation and mitigation

Both aluminum and titanium spatter dynamics were observed during LPBF. The underlying formation and propagation phenomena are consistent between the two materials. However, the differences in the melting/boiling point of the material altered the processing parameters that initiated the formation of different spatter. This indicates that the spatter formation map is dependent on the material being processed.

4. Conclusions

This work has distinguished five types of spatter produced in the LPBF process. The formation mechanism and features of each type of spatter are identified and quantitatively analyzed. The major conclusions are listed below:

1. Five types of spatter are observed and identified in the LPBF process: solid spatter, metallic jet spatter, agglomeration spatter, entrainment melting spatter, and defect induced spatter.

2. The formation mechanisms of five types of spatter were analyzed and described. Solid spatter is formed due to the intense vapor jet ejecting un-melted feedstock powders out of the powder bed. Metallic jet spatter is the detachment of liquid droplet from the melt pool resulting from the intensive vaporization induced depression zone/melt pool instability. Powder agglomeration spatter is formed through coalescing of multiple powders/spatters. Entrainment melting spatter is the melting and ejection of the entrained powders. Defect induced spatter is induced by large defects within the previously built layers.

3. The speed, size, and direction of metallic jet spatter, agglomeration spatter, and entrainment melting spatter were quantified. Metallic jet spatter exhibits the highest speed, powder agglomeration spatter has the largest size. The direction of the spatter highly depends on the depression zone geometry, which provides a potential way to determine the shape of the depression zone from spatter direction.

4. Types of spatter formed in LPBF process and their features depend on processing parameters (laser power, scan speed, and environmental pressure). A spatter formation map is constructed for AlSi10Mg alloy.

Acknowledgements

This work is funded by Honeywell Federal Manufacturing & Technologies (FM&T) and National Science Foundation (Award Number: 2002840). The authors would like to thank Alex Deriy at the APS for his help on the beamline experiments. This research used resources of the Advanced Photon Source, a U.S. Department of Energy (DOE) Office of Science User Facility operated for the DOE Office of Science by Argonne National Laboratory under Contract No. DE-AC02-06CH11357. All data prepared, analyzed and presented has been developed in a specific context of work and was prepared for internal evaluation and use pursuant to that work authorized under the referenced contract. Reference herein to any specific commercial product, process or service by trade name, trademark, manufacturer, or otherwise, does not necessarily constitute or imply its endorsement, recommendation, or favoring by the United States Government, any agency thereof or Honeywell Federal Manufacturing & Technologies, LLC. This publication has been authored by Honeywell Federal Manufacturing & Technologies under Contract No. DE-NA0002839 with the U.S. Department of Energy. The United States Government retains and the publisher, by accepting the article for publication, acknowledges that the United States Government retains a nonexclusive, paid up, irrevocable, world-wide license to publish or reproduce the published form of this manuscript, or allow others to do so, for the United States Government purposes.

References

[1] D.D. Gu, W. Meiners, K. Wissenbach, R. Poprawe, Laser additive manufacturing of

metallic components: materials, processes and mechanisms, Int. Mater. Rev. 57 (2013) 133–164.

[2] S.A. Khairallah, A.T. Anderson, A. Rubenchik, W.E. King, Laser powder-bed fusion additive manufacturing: Physics of complex melt flow and formation mechanisms of pores, spatter, and denudation zones, Acta Mater. 108 (2016) 36–45. https://doi.org/10.1016/j.actamat.2016.02.014.

[3] C.Y. Yap, C.K. Chua, Z.L. Dong, Z.H. Liu, D.Q. Zhang, L.E. Loh, S.L. Sing, Review of selective laser melting: Materials and applications, Am. Inst. Phys. 2 (2015) 01–21. https://doi.org/10.1063/1.4935926.

[4] A.A. W. E. King R. Ferencz, N. Hodge,, S.K. C. Kamath A. Rubencik, Laser powder bed fusion additive manufacturing of metals; physics, computational, and materials challenges, Acta Mater. 108 (2016) 36–45.

[5] W. Gao, Y. Zhang, D. Ramanujan, K. Ramani, Y. Chen, C.B. Williams, C.C.L. Wang, Y.C. Shin, S. Zhang, P.D. Zavattieri, The status, challenges, and future of additive manufacturing in engineering, Comput. Des. 69 (2015) 65–89. https://doi.org/10.1016/j.cad.2015.04.001.

[6] R. Esmaeilizadeh, U. Ali, A. Keshavarzkermani, Y. Mahmoodkhani, E. Marzbanrad, E. Toyserkani, On the effect of spatter particles distribution on the quality of Hastelloy X parts made by laser powder-bed fusion additive manufacturing, J. Manuf. Process. 37 (2019) 11–20. https://doi.org/10.1016/j.jmapro.2018.11.012.

[7] C. Barrett, C. Carradero, E. Harris, K. Rogers, E. MacDonald, B. Conner, Statistical analysis of spatter velocity with high-speed stereovision in laser powder bed fusion, Prog. Addit. Manuf. 4 (2019) 423–430. https://doi.org/10.1007/s40964-019-00094-6.

[8] A. Bin Anwar, I.H. Ibrahim, Q.C. Pham, Spatter transport by inert gas flow in selective laser melting: A simulation study, Powder Technol. 352 (2019) 103–116. https://doi.org/10.1016/j.powtec.2019.04.044.

[9] D. Wang, G. Ye, W. Dou, M. Zhang, Y. Yang, S. Mai, Y. Liu, Influence of spatter particles contamination on densification behavior and tensile properties of CoCrW manufactured by selective laser melting, Opt. Laser Technol. 121 (2020) 105678. https://doi.org/10.1016/j.optlastec.2019.105678.

[10] D. Galicki, B.C. Chakoumakos, S.P. Ringer, M. Eizadjou, C.J. Rawn, K. Nomoto, S.S. Babu, On the Formation of Spherical Metastable BCC Single Crystal Spatter Particles during Selective Laser Melting, Materialia. 9 (2020) 100584. https://doi.org/10.1016/j.mtla.2020.100584.

[11] C. Zhao, Q. Guo, X. Li, N. Parab, K. Fezzaa, W. Tan, L. Chen, T. Sun, Bulk-Explosion-Induced Metal Spattering during Laser Processing, Phys. Rev. X. 9 (2019) 21052. https://doi.org/10.1103/PhysRevX.9.021052.

[12] U. Ali, R. Esmaeilizadeh, F. Ahmed, D. Sarker, W. Muhammad, A. Keshavarzkermani, Y. Mahmoodkhani, E. Marzbanrad, E. Toyserkani, Identification and characterization of spatter particles and their effect on surface roughness, density and mechanical response of 17-4 PH stainless steel laser powder-bed fusion parts, Mater. Sci. Eng. A. 756 (2019) 98–107. https://doi.org/10.1016/j.msea.2019.04.026.

[13] A.T. Sutton, C.S. Kriewall, M.C. Leu, J.W. Newkirk, B. Brown, Characterization of laser spatter and condensate generated during the selective laser melting of 304L stainless steel powder, Addit. Manuf. 31 (2020) 100904. https://doi.org/10.1016/j.addma.2019.100904.

[14] A. Masmoudi, R. Bolot, C. Coddet, Investigation of the laser–powder–atmosphere interaction zone during the selective laser melting process, J. Mater. Process. Technol. 225 (2015) 122–132. https://doi.org/10.1016/j.jmatprotec.2015.05.008.

[15] V. Semak, A. Matsunawa, The role of reoil pressure in energy balance during laser materials processing, J. Phys. D. Appl. Phys. 30 (1997) 18.

[16] T.L.R.H.X.C.S.G.S. Pang, Localized boiling-induced spatters in the high-power laser welding of stainless steel: three-dimensional visualization and physical understanding, Appl. Phys. Rev. 124 (2018) 654.

[17] V. Gunenthiram, P. Peyre, M. Schneider, M. Dal, F. Coste, I. Koutiri, R. Fabbro, Experimental analysis of spatter generation and melt-pool behavior during the powder bed laser beam melting process, J. Mater. Process. Technol. 251 (2018) 376–386. https://doi.org/10.1016/j.jmatprotec.2017.08.012.

[18] Q. Guo, C. Zhao, L.I. Escano, Z. Young, L. Xiong, K. Fezzaa, W. Everhart, B. Brown, T. Sun, L. Chen, Transient dynamics of powder spattering in laser powder bed fusion additive manufacturing process revealed by in-situ high-speed high-energy x-ray imaging, Acta Mater. 151 (2018) 169–180. https://doi.org/10.1016/j.actamat.2018.03.036.

[19] M.J. Matthews, G. Guss, S.A. Khairallah, A.M. Rubenchik, P.J. Depond, W.E. King, Denudation of metal powder layers in laser powder bed fusion processes, Acta Mater. 114 (2016) 33–42. https://doi.org/10.1016/j.actamat.2016.05.017.

[20] D. Wang, S. Wu, F. Fu, S. Mai, Y. Yang, Y. Liu, C. Song, Corrigendum to “Mechanicsms and characteristics of spatter generation in SLM processing and its effect on the properties,” Mater. Des. 137 (2018) 33–37. https://doi.org/10.1016/j.matdes.2016.12.060 10.1016/j.matdes.2017.09.058.

[21] M. Taheri Andani, R. Dehghani, M.R. Karamooz-Ravari, R. Mirzaeifar, J. Ni, Spatter formation in selective laser melting process using multi-laser technology, Mater. Des. 131 (2017) 460–469. https://doi.org/10.1016/j.matdes.2017.06.040.

[22] Y. Liu, Y. Yang, S. Mai, D. Wang, C. Song, Investigation into spatter behavior during selective laser melting of AISI 316L stainless steel powder, Mater. Des. 87 (2015) 797–806. https://doi.org/10.1016/j.matdes.2015.08.086.

[23] M. Simonelli, C. Tuck, N.T. Aboulkhair, I. Maskery, I. Ashcroft, R.D. Wildman, R. Hague, A Study on the Laser Spatter and the Oxidation Reactions During Selective Laser Melting of 316L Stainless Steel, Al-Si10-Mg, and Ti-6Al-4V, Metall. Mater. Trans. A. 46 (2015) 3842–3851. https://doi.org/10.1007/s11661-015-2882-8.

[24] M.J. Zhang, G.Y. Chen, Y. Zhou, S.C. Li, H. Deng, Observation of spatter formation mechanisms in high-power fiber laser welding of thick plate, Appl. Surf. Sci. 280 (2013) 868–875. https://doi.org/10.1016/j.apsusc.2013.05.081.

[25] D.K.Y. Low, L. Li, A.G. Corfe, Charcteristics of spatter formation under the effect of different laser parameters during laser drilling, J. Mater. Process. Technol. 118 (2001)

179–186.

[26] P. Bidare, I. Bitharas, R.M. Ward, M.M. Attallah, A.J. Moore, Laser powder bed fusion in high-pressure atmospheres, Int. J. Adv. Manuf. Technol. 99 (2018) 543–555. https://doi.org/10.1007/s00170-018-2495-7.

[27] W.E. King, H.D. Barth, V.M. Castillo, G.F. Gallegos, J.W. Gibbs, D.E. Hahn, C. Kamath, A.M. Rubenchik, Observation of keyhole-mode laser melting in laser powder-bed fusion additive manufacturing, J. Mater. Process. Technol. 214 (2014) 2915–2925. https://doi.org/10.1016/j.jmatprotec.2014.06.005.

[28] B. Song, S. Dong, B. Zhang, H. Liao, C. Coddet, Effects of processing parameters on microstructure and mechanical property of selective laser melted Ti6Al4V, Mater. Des. 35 (2012) 120–125. https://doi.org/10.1016/j.matdes.2011.09.051.

[29] B. Zhang, L. Dembinski, C. Coddet, The study of the laser parameters and environment variables effect on mechanical properties of high compact parts elaborated by selective laser melting 316L powder, Mater. Sci. Eng. A. 584 (2013) 21–31. https://doi.org/10.1016/j.msea.2013.06.055.

[30] T.M. Mower, M.J. Long, Mechanical behavior of additive manufactured, powder-bed laser-fused materials, Mater. Sci. Eng. A. 651 (2015) 198–213. https://doi.org/10.1016/j.msea.2015.10.068.

[31] M. Grasso, B.M. Colosimo, Process defects andin situmonitoring methods in metal powder bed fusion: a review, Meas. Sci. Technol. 28 (2017) 44005. https://doi.org/10.1088/1361-6501/aa5c4f.

[32] J. Yin, L.L. Yang, X. Yang, H. Zhu, D. Wang, L. Ke, Z. Wang, G. Wang, X. Zeng, High-power laser-matter interaction during laser powder bed fusion, Addit. Manuf. 29 (2019) 100778. https://doi.org/10.1016/j.addma.2019.100778.

[33] X. Zhang, B. Cheng, C. Tuffile, Simulation study of the spatter removal process and optimization design of gas flow system in laser powder bed fusion, Addit. Manuf. 32 (2020) 101049. https://doi.org/10.1016/j.addma.2020.101049.

[34] S.A. Khairallah, A.A. Martin, J.R.I. Lee, G. Guss, N.P. Calta, J.A. Hammons, M.H. Nielsen, K. Chaput, E. Schwalbach, M.N. Shah, M.G. Chapman, T.M. Willey, A.M. Rubenchik, A.T. Anderson, Y.M. Wang, M.J. Matthews, W.E. King, Controlling interdependent meso-nanosecond dynamics and defect generation in metal 3D printing, Science (80-.). 368 (2020) 660–665.